Hindawi
Advances in Materials Science and Engineering
Volume 2019, Article ID 6024876, 12 pages
https://doi.org/10.1155/2019/6024876

Research Article

Structural and Oxidative Properties of Manganese Incorporated Mesostructure Silica for Methane Oxidation

Rihem Dardouri,[1] **Anis Gannouni**,[2] **and Mongia Saïd Zina**[1]

[1]*Laboratoire de Chimie des Matériaux et Catalyse, Faculté des Sciences de Tunis, Campus Universitaire, Tunis 2092, Tunisia*
[2]*Université de Carthage, Institut Préparatoire Aux Etudes D'ingénieurs de Nabeul, Nabeul, Tunisia*

Correspondence should be addressed to Rihem Dardouri; rihemda1@gmail.com

Received 15 July 2018; Revised 29 November 2018; Accepted 6 December 2018; Published 2 January 2019

Academic Editor: Alfredo Juan

Manganese catalysts containing templated mesostructured porous silica were prepared using different methods of preparation, namely, the direct hydrothermal (DHT), solid-state ion exchange (SSI), template ion exchange (TIE), and impregnation (Imp) methods. The physical-chemical properties of materials were characterized by X-ray diffraction (XRD), N_2 adsorption-desorption, FT-IR, TEM, EDX, UV-Vis, EPR, and H_2 TPR techniques. The results of this study indicate that the obtained catalysts retained their hexagonal mesopore structure after introducing Mn into MCM-41. On the contrary, the crystalline phase of manganese oxide was stabilized on the external surface and inside the mesoporosity of the MCM-41 and seems to be dependent on the synthesis method used. Catalytic performances of synthesized materials were then investigated in methane oxidation at atmospheric pressure. The results showed that the metal loading and catalysts synthesis procedure influence the catalytic performance of the obtained materials. Moreover, the activity of the catalyst depends on the crystalline phase and particularly on the environment of the active phase.

1. Introduction

Given the global energy consumption and the decline of fossil fuels such as petroleum and charcoal, interest has been focused on methane, the major component of natural gas because of large world reserves and low level of impurities [1]. Nowadays, natural gas exists in the engines of natural gas vehicles and stationary gas turbines replacing gasoline and diesel since its simple composition makes it easier to achieve the complete combustion.

However, the conventional flame combustion process of methane produces emissions that are harmful to the environment, namely, nitrogen oxides (NO*x*) and unburned hydrocarbons (UHC) which is a powerful greenhouse gas that contributes to global warming, it has a more powerful impact of about 25 times on the greenhouse effect than CO_2 [2]. Therefore, the use of a catalytic route has proved to be an alternative way to overcome this inconveniency and in order to increase the performance of the methane combustion, highly efficient and inexpensive catalysts are needed.

As pointed out in several studies, supported noble metals were first considered and investigated for the methane oxidation process [3]. These metals are the most promising to catalyze the total oxidation of methane in the temperature range 300–700°C [4]. In particular, Pd-based catalysts were found among the most active ones to be effective in this reaction compared to other metals which exhibit high volatility, making them less attractive for the combustion of light alkanes because of reaching high temperatures during the combustion reaction [5, 6].

Nevertheless, catalysts based on transition metals such as Co, Mn, Cu, and Fe [7, 8], which are marked by high electron mobility and several oxidation states, become appealing in recent decades due to the high cost of noble metals and their poor resistance to thermal deactivation and poisoning.

Among the widely used transition metals, manganese was found to be effective in improving the catalytic activity in oxidation reaction such as the oxidation of methane [9], cyclohexene [10], ethyl acetate [11], toluene [12], and so on. It is commonly accepted that the catalytic properties of

MnOx based catalysts is related to the high oxygen storage capacity of manganese and its ability to form oxides with variable oxidation states [13]. Thus, it was reported that the best catalytic performance was attributed to the highest valence state of manganese species. In this context, it was found that the catalytic activity of manganese is frequently correlated to the Mn^n/Mn^{n-1} content. In fact, it turned out that Mn^{4+} sites are more active than Mn^{3+} sites for methane oxidation [13, 14].

Hu et al. [9] compared the performances of Mn-based catalysts on different supports (Al_2O_3, SiO_2, and TiO_2) for methane combustion, and manganese oxide supported on Al_2O_3 was found to be more active owing to the high rate of mobile oxygen in the support and the increase of acidity which enhances the catalytic activity. Moreover, the metal content can also influence the catalytic activity of materials in methane oxidation as was investigated by Laugel et al. [15] who showed that Mn/SBA-15 catalyst with a high loading of manganese oxide (30 wt.%) leads to a decrease in activity compared with the catalysts at lower Mn loading (7 wt.%). In addition, the study of the effect of precursor was reported by many authors; Pérez et al. [11] showed that Mn permanganate and Mn nitrate are more active than Mn acetate in the total oxidation of ethyl acetate. On the contrary, Döbber et al. [16] proved that the activity of MnOx for the total oxidation of methane is influenced by the dispersion of the MnOx species which depends on the method of preparation. They found that highly dispersed supported MnOx species were obtained using the precipitation method compared with that using the wet impregnation method.

There is a general agreement that the catalytic activity for methane combustion reaction depends on several factors among other interaction metal/support [17]. Therefore, choosing the most appropriate support is a crucial matter since it is responsible for the nature and dispersion of the active species which depends also on catalyst preparation methods. Therefore, in the last few years, there was a particular interest in choosing mesoporous silica such as MCM-41 and SBA-15 as a support owing to their high surface area, large and uniform pore structure, well-defined nanosize channels, and high metal dispersion capabilities [18, 19].

In this work, special attention will be paid to determine how the method of preparation of catalysts and the metal loading can affect the textural, structural, and catalytic properties of manganese containing mesoporous LUS silica-type MCM-41 for methane combustion.

2. Experimental

2.1. Reactants. Ludox HS-40 (40% SiO_2, Aldrich), sodium hydroxide (Acros), cetyltrimethylammonium p-toluenesulfonate, (CTATos; >99% Merck), ammonium nitrate (95%, Alfa Aesar), manganese (II) acetate (99%, Aldrich), and ethanol (96%, Elvetec). The sodium silicate solution was prepared as follows: Ludox HS-40 (187 mL) was added to sodium hydroxide (32 g) in deionized water (800 mL) and stirred at 40°C for 24 h.

2.2. Catalysts Preparation

2.2.1. Synthesis of LUS. The support was synthesized according to the procedure reported for mesoporous-templated silicas LUS (Laval University silica) that uses a surfactant (CTATos) as template wherein the cationic surfactant is a tosylate salt instead of a bromide or chloride salt as in the case of the conventional preparation of MCM-41 described in the literature [20]. A sodium silicate solution (80 mL) was stirred at 60°C for 1 h simultaneously; a second solution of cetyltrimethylammonium p-toluenesulfonate (CTATos, 3.2 g) was dissolved in deionized water (120 mL) and kept under stirring at 60°C for 1 h. The first solution was added dropwise to the second one and then stirred at 60°C for 2 h. The resulting sol-gel was transferred in an autoclave and heated at 130°C during 20 h. After filtration, washing with deionized water (about 150 mL), and drying at 80°C, about 5 g of solid was obtained.

2.2.2. Partial Surfactant Extraction of LUS. In order to obtain the amount of the surfactant ions (CTA^+) in the support equal to 42%, we opted for the ion exchange method performed according to the experimental protocol described by Lang and Tuel [21] using an alcoholic solution of ammonium nitrate. 3 g of LUS is suspended in 120 mL of ethanol (96%) containing 0.52 g of NH_4NO_3. The resulting mixture was stirred at 60°C for 45 min. After filtration and washing with ethanol (3 × 70 mL), the powder was dried at 80°C overnight to obtain the as-synthesized sample LUS_{42}.

2.2.3. Metal Incorporation: MnLUS Materials. The nominal manganese-containing catalyst (%wt. Mn 7, 15, and 30%) was elaborated via the direct hydrothermal synthesis (DHT), template ion exchange (TIE), wetness impregnation techniques (Imp), and solid-state ion exchange (SSI) method.

(1) The Direct Hydrothermal (DHT) Synthesis. An aqueous solution of manganese (II) acetate was added to the mixture of 3.2 g of CTATos. The sodium silicate solution was added dropwise to the first solution and stirred at 60°C for 2 h. After hydrothermal synthesis at 130°C during 20 h, a pale pink powder was filtered, washed with water, and dried at 80°C overnight to give the synthesized sample $MnLUS_{DHT}$.

(2) The Template Ion Exchange (TIE) Procedure. The partially extracted support (LUS_{42}) was dissolved in an aqueous solution of $Mn(OAc)_2$ (120 mL). The mixture was stirred at 80°C for 1 h. After filtration and washing with deionized water, the solid $MnLUS_{TIE}$ was dried for 20 h at 80°C.

The reaction equation shows the exchange made between the Mn^{2+} ion and the deprotonated silanol groups of the surface (SiO^-) with the charge is balanced by ions of the surfactant molecule (CTA^+):

$$2\{SiO^-, CTA^+\} + \{Mn^{2+}, 2CH_3COO^-\} = \{2SiO^-, Mn^{2+}\} + 2\{CH_3COO^-, CTA^+\}. \quad (1)$$

(3) The Impregnation (Imp) Process. 2 g of calcined LUS is dissolved in an aqueous solution of manganese acetate. The mixture was kept under vigorous stirring for 4 h at 50°C. The solvent was then removed by the rotary evaporator at 50°C followed by drying overnight at 120°C to obtain $MnLUS_{Imp}$.

(4) The Solid-State Ion Exchange (SSI) Method. The $MnLUS_{SSI}$ was prepared by the solid-state ion exchange method as described elsewhere [22, 23]. The calcined LUS was intimately mixed and ground in a mortar with the desired quantity of $Mn(OAc)_2$. The finely ground powder was poured in a fixed bed placed in a U-shaped microreactor and then treated in helium flow (30 cm^3/min) during 18 h at 500°C (1°C/min).

All the samples were treated under pure dioxygen at a flow rate of 30 cm^3/min and a temperature ramp of 1°C/min up to 550°C for 8 h. The solids were kept in sealed vials.

2.3. Characterization Techniques

2.3.1. X-Ray Powder Diffraction. XRD patterns were collected on automated diffractometer Philips Panalytical using the CuKα radiation (λ = 1.54056 Å) and a nickel monochromator. The 2θ range 0.8–10° was scanned at the step of 0.02 s^{-1}. The primary mesopore diameter (w_d) was calculated from interplanar d-spacing of the most intense (100) peak in the XRD pattern using the following equation [24]:

$$W_d = c \cdot d \left(\frac{\rho v_p}{1 + \rho v_p} \right)^{1/2}, \quad (2)$$

where ρ is the pore wall density supposed to be equal to that of amorphous silica 2.2 g/cm^3 and c is a constant equal to 1.213 for cylindrical pores.

2.3.2. Fourier-Transformed Infrared. FT-IR spectra were taken from pressed pellets with KBr under a pressure of 6.10^5 Pa. The spectra were recorded using the PerkinElmer FT-IR spectrometer in the range of wave numbers 400–4000 cm^{-1}.

2.3.3. UV-Visible Spectroscopy. Solid UV-visible spectra were recorded applying a JASCO V-670 (JASCO) spectrophotometer in the diffuse reflectance mode. The selected recording parameters comprised a data interval of 1 nm, a spectral bandwidth of 5.0 nm, and a scan speed of 400 nm·min^{-1}.

2.3.4. N_2 Adsorption/Desorption. Surface areas of samples were determined from the N_2 sorption isotherms at 77 K with the BET method using a Micromeritics ASAP 2000 Analyzer. Before measurements, the samples were outgassed for 4 h at 200°C under vacuum. The total pore volume was estimated by means of the total amount of adsorbed gas at relative pressure P/P^o = 0.98.

The pore-size distributions were determined by the BJH method, using the desorption branches of isotherms.

2.3.5. H_2 Temperature-Programmed Reduction. The analyses were performed using a Micromeritics AutoChem 2920 unit. 50 mg of sample is placed in a U-shaped quartz cell. Before measurement, the sample was activated and flowing O_2 (5 vol.%)/He at 300°C with a heating rate of 10°C/ min and a flow rate D = 30 cm^3/min and then cooled down to 30°C. The reduction was performed under a mixed gas stream of 5% H_2/He with a flow rate of 30 cm^3/min and a temperature rise of about 10°C/ min to reach the final value of 700°C.

2.3.6. EPR Spectroscopy. This technique was used to study the oxidation states of manganese ions in MnLUS samples and to elucidate their local electronic structure. EPR spectra were recorded using a Bruker Elexsys e500 X-band (9.4 GHz) spectrometer operating at 100 kHz modulation frequency with a standard rectangular cavity.

2.3.7. Transmission Electron Microscopy (TEM). The morphology of the samples was performed on TEM FEI TECNAI G2 Ultra-Twin instrument operating at 200 kV. The sample was first ultrasonically dispersed in ethanol before deposition on a copper grid coated with a porous carbon film.

2.4. Catalytic Test. The catalytic test was performed using 0.1 g catalyst loaded in U-shaped dynamic microreactor (catalytic bed: id, 10 mm, and length, 6 mm). The reactor, operating under atmospheric pressure, was placed in a tubular furnace equipped with a temperature programmer and the reaction temperature was controlled with a K-type thermocouple. The reaction mixture which included CH_4, O_2, and inert (He) gases (1 vol% CH_4 and 4 vol% O_2 in helium) was fed into the reactor at a total flow of 100 ml min^{-1}. The temperature of the catalysts was increased from 450°C to 700°C at the rate of 5°C min^{-1}, and the conversion of CH_4 was measured at an interval of 25°C (holding time 30 min). The reactants and reaction products were analyzed using a gas chromatograph equipped with a thermal conduction detector. A Porapak Q column was used to separate the reaction products. The thermal stability tests were performed maintaining the reaction temperature at 700°C for 200 min.

The CH_4 conversion (CH_4%) was calculated from the experimental concentrations of the reagents and products; the turnover frequency of TOF_{Mn} and the specific rate were calculated using the following equations [25, 26]:

$$\text{methane conversion}\,(\%) = \frac{\text{moles } CH_4 \text{ in} - \text{moles } CH_4 \text{ out}}{\text{moles } CH_4 \text{ in}} \cdot 100,$$

$$\text{TOF}_{\text{Mn}} = \frac{C_{\text{methane}} \cdot \text{MC} \cdot V_{\text{gas}}}{n_{\text{Mn}}} \left(s^{-1}\right),$$

$$\text{specific rate} = \frac{V_{\text{methane}} \cdot \text{MC}}{22400 \cdot m} \left(\text{mol} \cdot g_{\text{cat}}^{-1} \cdot s^{-1}\right), \tag{3}$$

where C_{methane} is the methane concentration in the inlet gas; MC is the methane conversion; n_{Mn} is the molar amounts of Mn; V_{gas} represents the total molar flow rate; V_{methane} is the flow rate of CH_4, and m is the mass of the catalyst (g).

3. Result and Discussion

3.1. X-Ray Diffraction. The XRD patterns of the obtained materials are shown in Figure 1. All MnLUS catalysts revealed four well-resolved peaks corresponding to the diffraction caused by the lattice planes (100), (110), (200), and (210) which is characteristic of mesoporous silica with a well-ordered hexagonal porous array [27, 28]. The distance between two adjacent pore centers in the hexagonal structure of LUS and the lattice parameters (a_o) are gathered in Table 1, and all the above results are in good agreement with the literature results [29, 30].

The intensity of all the diffraction peak of MnLUS was decreased compared to the diffraction pattern of the support (LUS) indicating that the metal-support interaction causing a slight deformation in the channels due to the introduction of Mn in the mesopores (Table 2).

The X-ray diffraction patterns at high angles exhibit a broad diffraction peak, centered approximately at $2\theta = 23^\circ$, which is due to amorphous silica. The XRD pattern of different catalysts showed no peak characteristic of manganese oxide which could be explained by a very high metal dispersion, except $\text{MnLUS}_{\text{SSI}}$ (Figure 1(b) (E)) which reveal three main diffraction peaks at 28°, 32°, and 36° that can be related to the formation of manganese oxides (MnO_x), probably MnO_2 (pyrolusite, JCPDF 72-1984) and/or Mn_2O_3 (Bixbite, JCPDF 24-508). The observation of these phases agrees with other literature reports [31].

3.2. N_2 Adsorption-Desorption Analysis. As shown in Figure 2, N_2 sorption isotherms of MnLUS catalysts exhibited type-IV isotherm profiles characteristic of a typical mesoporous material, which confirm the maintenance of the ordered structure after manganese incorporation. The textural properties of LUS and MnLUS samples are listed in Table 1. The obtained results show that all these materials display a narrow pore-size distribution and high surface area. The incorporation of metal in the nanochannels of the siliceous matrix was confirmed by the decreasing of S_{BET} and pore volume following the introduction of manganese species into the support [32]. It should be noted that, for the sample prepared by the template ion exchange method, $\text{MnLUS}_{\text{TIE}}$, surface area, and pore volume increase compared with the parent LUS. A similar result was observed by Derylo-Marczewska et al. [33] who suggested that such result could be due to a partial collapse in the structure caused by the rate of the exchange process. Moreover, an increase of pore diameter showed that larger cavities were formed like in the pure silica support [19].

The pore-size distributions of different materials are summarized in Figure 2(b); all catalysts show bimodal distribution indicating the uniformity of pore systems, except $\text{MnLUS}_{\text{TIE}}$ whish has a trimodal pore-size distribution, and a similar result was found by Coville et al. [34].

3.3. FT-IR Spectroscopy. The framework vibration for different materials was analyzed by FT-IR. The broad band at 3500 cm^{-1} correspond to surface silanol groups, whereas deformational vibrations of adsorbed water molecules is assigned to the band at 1650 cm^{-1}. The bands at 1030–1080 cm^{-1} and that located at 800 cm^{-1} are attributed, respectively, to the asymmetric and symmetric stretching vibrations of Si–O–Si bridges. While the band at 450–460 cm^{-1} is due to Si–O bending vibrations.

The changes of band intensity located at 975 cm^{-1} which is assigned to stretching vibration of the Si–O–Me linkage pointed out the incorporation of manganese into the silica framework. This increase in intensity should be due to the increase of the mean Si–O distance in the walls caused by the substitution of the small silicon (radius 40 pm) by the larger size of Mn^{2+} (radius 83 pm) [35].

3.4. H_2 TPR Analysis. The oxidation states of manganese species and the significant reduction differences between samples were studied by H_2 TPR, and the curves are shown in Figure 3. The reduction of manganese oxides is often described by the following sequential process: $MnO_2 \longrightarrow Mn_2O_3 \longrightarrow Mn_3O_4 \longrightarrow MnO$. Nevertheless, all the samples showed two distinct peaks: the first reduction peaks located in the range of 200–450°C is attributed to the reduction reactions $MnO_2/Mn_2O_3 \longrightarrow Mn_3O_4$, and the second one at higher temperature in the range of 450–650°C due to the reduction of the Mn_3O_4 phase to MnO [36]. The manganese oxide species in the samples prepared by hydrothermal, template ion exchange and impregnation method are more difficult to reduce. In addition, the broadening of the TPR peaks observed can be assigned to the presence of species with different reducibilities, resulting from a different strength of Mn–O interactions. In the case of $\text{MnLUS}_{\text{SSI}}$ catalyst, two intense peaks in the temperature range of 300–400°C are observed which indicate the formation of a mixture of MnO_2 and Mn_2O_3. Furthermore, there are slight shifts toward lower temperature for the reduction peaks; such behaviors suggest that the interaction of MnO_2 with support became weaker. These results are in good correlation with those obtained by XRD.

3.5. UV-Vis Spectroscopy. The state of Mn^{n+} in the MnO_x species was investigated by diffuse reflection spectroscopy, and the results are shown in Figure 4. The MnLUS samples

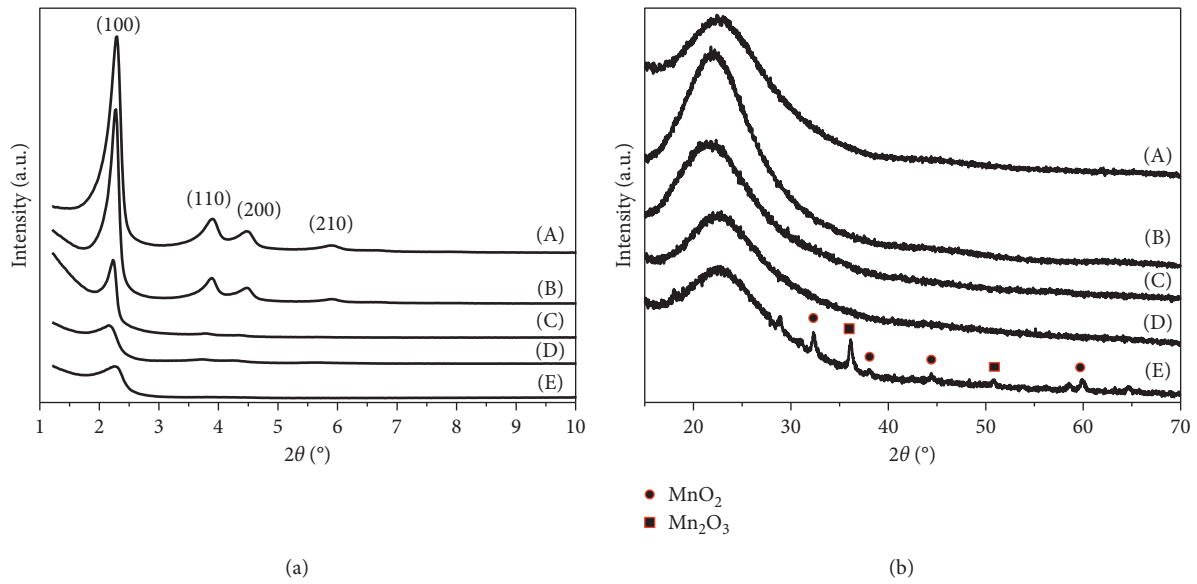

Figure 1: XRD patterns (a) at low diffraction angles of (A) LUS and MnLUS (7 wt.%), (B) $MnLUS_{SSI}$, (C) $MnLUS_{TIE}$, (D) $MnLUS_{DHT}$, and (E) $MnLUS_{Imp}$ and (b) at high diffraction angles of (A) LUS, (B) $MnLUS_{TIE}$, (C) $MnLUS_{DHT}$, (D) $MnLUS_{Imp}$, and (E) $MnLUS_{SSI}$.

Table 1: Physicochemical characterization of MnLUS catalysts.

Material	d_{100} (nm)[a]	a_o (nm)[b]	S^c_{BET} (m^2/g)	Pore size[c], D (nm)	V^c_p (cm^3/g)	w_d (nm)[d]	Total H_2 consumption ($mmol_{H2}$/gcat)[e]
LUS	4	4.61	1038	3.17	1.04	4.04	—
$MnLUS_{DHT}$	3.90	4.70	658	4.63	0.85	3.80	0.83
$MnLUS_{TIE}$	3.80	4.58	1074	5.10	1.61	4.07	0.87
$MnLUS_{SSI}$	3.90	4.41	914	3.23	0.92	3.87	1.08
$MnLUS_{Imp}$	3.82	4.50	929	2.92	0.63	3.53	0.53

[a]Values obtained from XRD studies. [b]$a_o = 2 \times d_{100}/\sqrt{3}$. [c]Values obtained from N_2 adsorption results. [d]$W_d = c \times d(\rho v_p/1 + \rho v_p)^{1/2}$. [e]Values obtained from H_2 TPR studies.

Table 2: Activity results for the catalytic oxidation of methane over the MnLUS catalysts.

Catalysts	% wt. Mn[a]	TOF (s^{-1})[b]	Specific rate, r ($10^4 \times$ mol $g^{-1}_{cat} \cdot s^{-1}$)[c]	MC[d]
$MnLUS_{DHT}$	7.8	0.051	3.7	57
$MnLUS_{TIE}$	5.6	0.037	2.7	43
$MnLUS_{Imp}$	5.4	0.039	2.9	41
Mn_7LUS_{SSI}	6.7	0.025	1.8	27
$Mn_{15}LU_{SSI}$	14.6	0.021	3.3	47
$Mn_{30}LUS_{SSI}$	29.3	0.018	5.7	75

[a]Values obtained from ICP elemental analysis. [b]Turnover Frequency (TOF) calculated at 700°C. [c]Specific rate calculated at 700°C. [d]Methane conversion at 700°C.

exhibited several bands at 255, 270, 320, 400, and 500 nm. The band at ca. 255 nm corresponds to $O^{2-} \longrightarrow Mn^{2+}$ charge transfer transition [37, 38]. While the charge transfer transition $O^{2-} \longrightarrow Mn^{4+}$, which is presented in MnO_2, was confirmed by the band at ca. 310–350 nm, and the one at ca. 400–500 nm is assigned to $O^{2-} \longrightarrow Mn^{3+}$ [39]. Thereby, MnLUS is mainly made up of a mixture of Mn^{3+}, Mn^{4+}, and Mn^{2+} oxo species.

For the $MnLUS_{DHT}$ sample, the spectra are characterized by an absorption band near 320 nm which is assigned to the charge transfer transition of $O^{2-} \longrightarrow Mn^{3+}$ in Mn_3O_4 in which Mn was octahedronally coordinated with oxygen [40]. However, MnO exhibited an absorption peak at 255 nm. The intense band observed at lower wavelength (270 nm) in the case of $MnLUS_{SSI}$ catalyst is perhaps due to the charge transfer transition of $O^{2-} \longrightarrow Mn^{3+}$ in the tetrahedral coordination within the framework of LUS. On the contrary, the spectra of $MnLUS_{TIE}$ and $MnLUS_{Imp}$ samples present an absorption band between 400 and 500 nm which could be due to charge transfer transitions of Mn^{3+}.

3.6. EPR Spectroscopy. Figure 5 shows EPR spectra of MnLUS samples at 120 K. $MnLUS_{SSI}$ and $MnLUS_{Imp}$ display a typical Mn(II) EPR spectrum characterized by six hyperfine lines centered on $g = 2.00$ and which correspond to

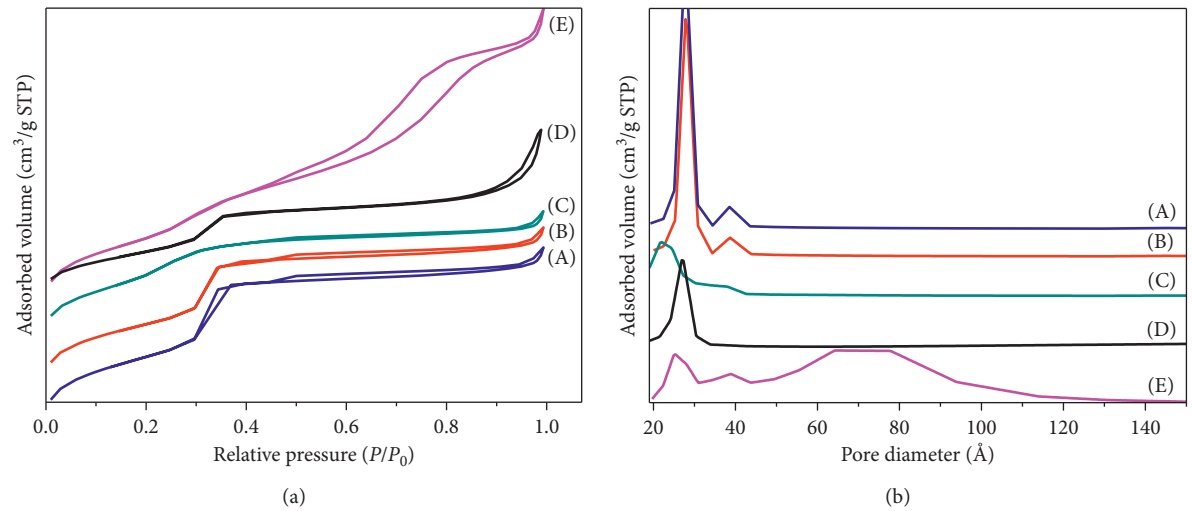

FIGURE 2: (a) N_2 adsorption-desorption isotherms at 77 K and (b) BJH pore-size distributions of (A) LUS and MnLUS (7 wt.%), (B) $MnLUS_{SSI}$, (C) $MnLUS_{Imp}$, (D) $MnLUS_{DHT}$, and (E) $MnLUS_{TIE}$.

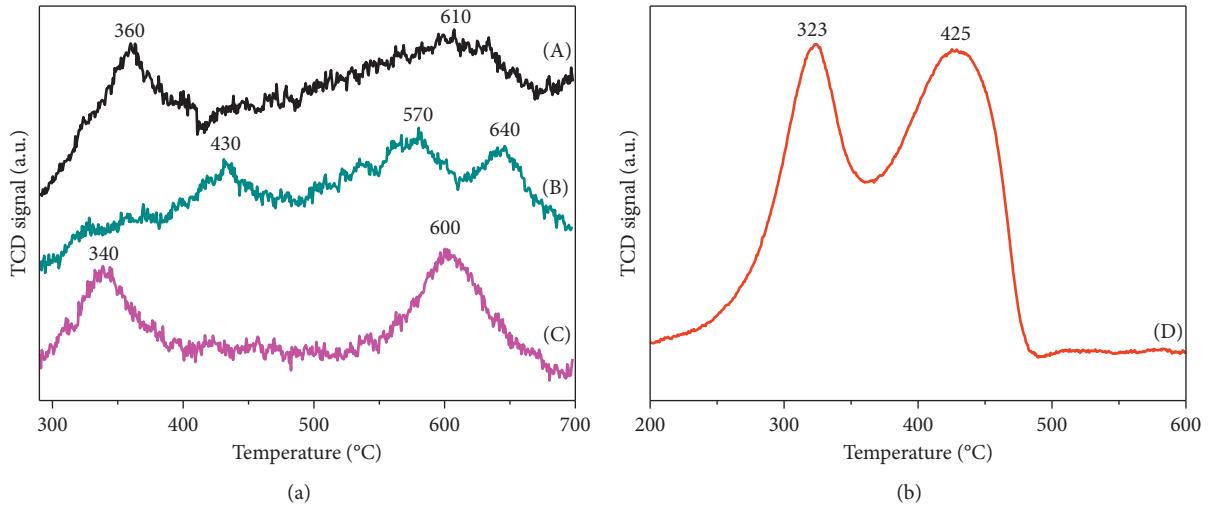

FIGURE 3: H_2 TPR profiles of MnLUS (7 wt.%) catalysts: (A) $MnLUS_{DHT}$, (B) $MnLUS_{Imp}$, (C) $MnLUS_{TIE}$, and (D) $MnLUS_{SSI}$.

extraframework Mn^{2+} species in the octahedral environment of silica oxygen. Furthermore, these bands were non-symmetric, indicating that the octahedral ligand field, created by oxygen framework, had suffered a tetrahedral deformation by the Jahn–Teller effect. Mn^{3+} is non-Kramers ion ($3\,d^4$, $S = 2$), and it does not show EPR signals at X-band frequency [41].

3.7. TEM/EDX Analysis. The TEM images of $MnLUS_{DHT}$ (7% wt. Mn), $MnLUS_{SSI}$ (15% and 30% wt. Mn), and $MnLUS_{Imp}$ (15% wt. Mn) samples are shown in Figure 6. It is clear that all the materials have a regular hexagonal arrangement of the channels with a uniform pore-size which proves that Mn oxide clusters did not disturb the mesoporous structure. TEM observations of $MnLUS_{SSI}$ present large aggregates of MnO_x outside the mesoporous silica channels on the external surface indicating the weak interaction metal-support which is in agreement with TPR and XRD results. Moreover, the pore size agrees with the value determined by N_2 adsorption (3.2 nm).

The results of EDX measurements confirmed the incorporation of manganese into mesoporous material. Several EDX analyses were performed on different parts of the samples indicating that manganese distribution was non-homogenous in the case of the $MnLUS_{SSI}$ sample. However, TEM images of $MnLUS_{Imp}$ and $MnLUS_{DHT}$ samples show the pores as black dots in the image in some case, while in some other occasion, white dots are observed. This is a univocal indication that some of the pores are empty and some other are blocked with MnO_x. The EDX analysis of $MnLUS_{Imp}$ and $MnLUS_{DHT}$ suggested that manganese is uniformly dispersed on inner surface of the LUS channel. Therefore, it was believed that the ordered mesoporous structures were maintained after incorporating manganese species into LUS.

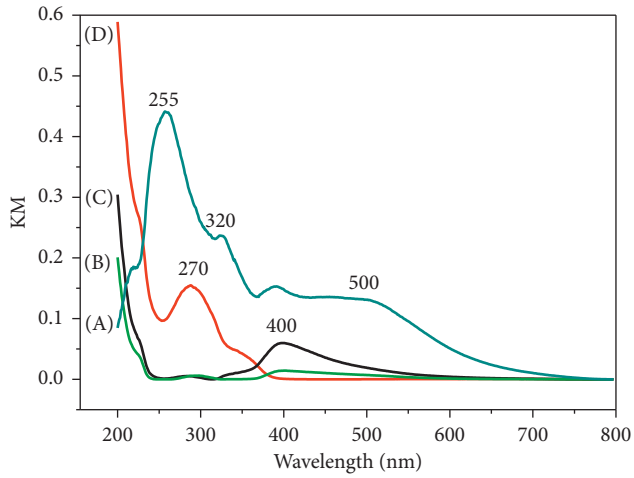

FIGURE 4: UV-Vis spectra of MnLUS (7wt.%) samples prepared with different methods of procedure (a) $MnLUS_{DHT}$, (b) $MnLUS_{TIE}$, (c) $MnLUS_{Imp}$, and (d) $MnLUS_{SSI}$.

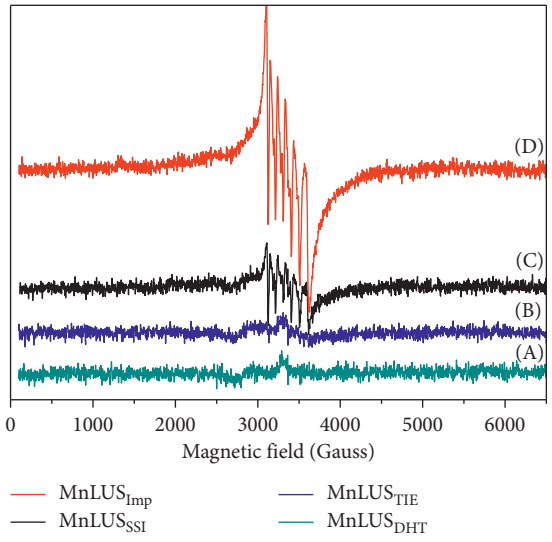

FIGURE 5: EPR spectra at 120 K of MnLUS samples (7 wt.%): (a) $MnLUS_{DHT}$, (b) $MnLUS_{TIE}$, (c) $MnLUS_{SSI}$, and (d) $MnLUS_{Imp}$.

4. Methane Oxidation Catalytic Test

The light-off curves of methane total combustion are reported for all the catalysts on Figure 7. As expected, during all catalytic activity tests, CO_2 was detected as the only carbon containing reaction product, indicating the complete oxidation of CH_4. The thermal stability of MnLUS catalysts was performed for on-stream periods of approximately 200 min (Supplementary Figure S1). A weak loss of activity (≈ 5%) was observed for all samples after 30 min.

The methane conversion as a function of temperature of MnLUS catalysts prepared with different methods of preparation, and the same manganese loading is presented in Figure 7(a). The obtained results indicate that, for low metal content, $MnLUS_{DHT}$ was more active than the other samples. Otherwise, the catalysts obtained by TIE and impregnation methods show comparable activity when the one that was prepared according to the solid-state ion exchange method ($MnLUS_{SSI}$) was less active most probably because of the weak metal-support interaction, causing difficulty in the dissociative adsorption of methane. It is worth noting that there is no correlation between catalytic activity and changes in specific surface area of the investigated samples. Such result suggests a predominant role of the environment of the active phase at determining catalytic performance.

In fact, it was established that catalytic activity increases when the pair Mn^{3+}/Mn^{4+} coexists in the structure of the oxide [42], and according to the results obtained by UV and TPR, $MnLUS_{DHT}$ is made up of a mixture of Mn^{3+} and Mn^{4+} oxo species. Indeed, the spectroscopic studies of Mn-MCM-41 materials prepared by hydrothermal method pointed to the coexistence of Mn^{2+} and Mn^{3+} ions coordinated with Si(IV) by disordered octahedral or tetrahedral environments and partial substitution of Si^{4+} in the framework position by Mn^{3+} as was reported earlier [43]. Moreover, Zhang et al. [40] characterized the local environment of manganese in MCM-41 synthesized by the direct hydrothermal (DHT) method, and they suggested that Mn^{2+} and Mn^{3+} coexisted in the Mn-MCM-41 materials and a large part of manganese atoms could be incorporated into the framework of MCM-41.

It is thus quite clear that the coexistence of Mn on the surface of mesoporous channels and those incorporated inside the framework generate catalytically active sites and were beneficial for the observed catalytic behavior.

On the contrary, the catalytic performance of $MnLUS_{SSI}$ synthesized by the solid-state ion exchange method with different manganese content was reported in Figure 7(b). It is clearly seen that an increase in Mn loading from 7% to 30% wt. leads to an increase in activity.

In fact, Derylo-Marczewska et al. [33] have reported that an increase in Mn loading causes an increase in the amount of Mn^{3+} and Mn^{4+} species. Furthermore, Cracium [44] found that Mn was present in mixed MnO_2/Mn_2O_3 crystalline phases on catalysts with high Mn loading and as a single MnO_2 phase on catalysts with low Mn loading.

According to TEM images, manganese at high loading in $MnLUS_{SSI}$ tends to form large aggregates. In contrast, $MnLUS_{Imp}$ reveals a homogenous dispersion of metal particles within the channels of mesoporous silica. Thus, we suggest that both particles sizes and dispersion play an important role in the catalytic activity of MnO_x in methane combustion. In fact, some authors obtained similar results on Al_2O_3 supported manganese oxide catalysts with different Mn content for the hydrocarbons combustion reaction [9, 34]. According to these authors, it appears that, in Mn loading, active component particles vary reciprocally with dispersion; indeed, for the catalyst with higher Mn content, active component particles were bigger and their dispersion was lower.

It should be noted that, at high manganese contents, the solid-state ion exchange method shows the better activity comparing with other method of preparation. It is generally believed that, for manganese oxides, the catalytic activity is

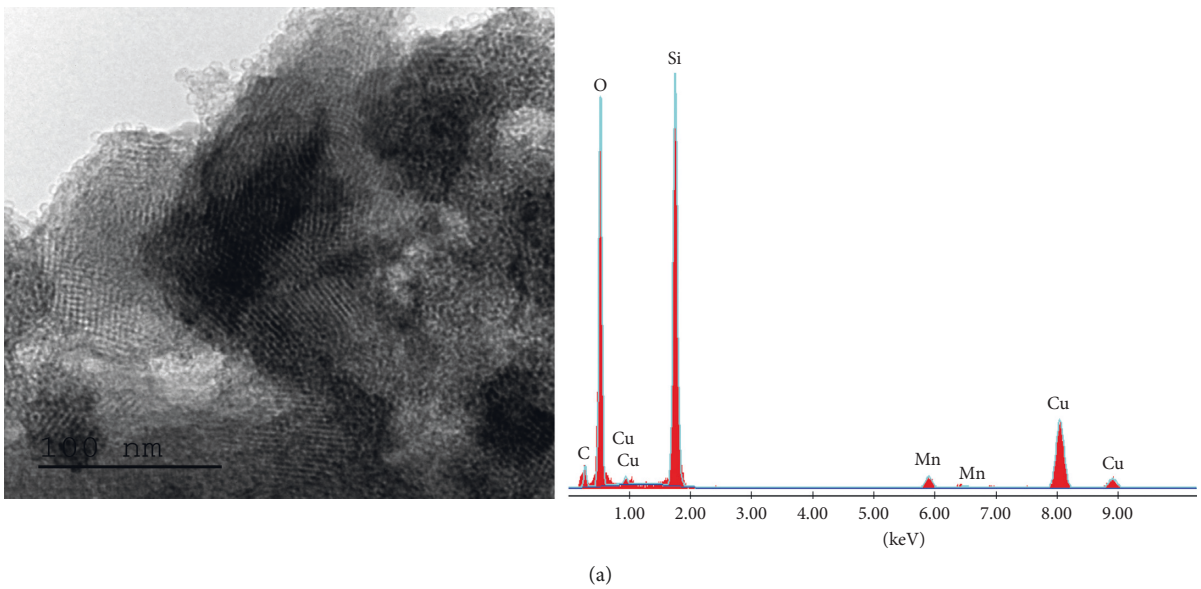

(a)

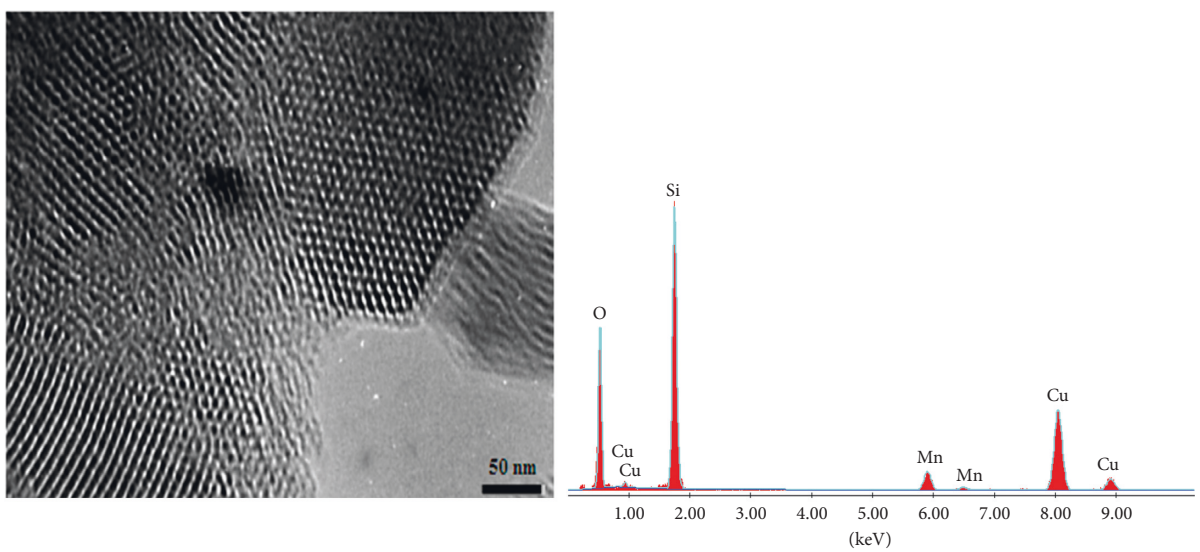

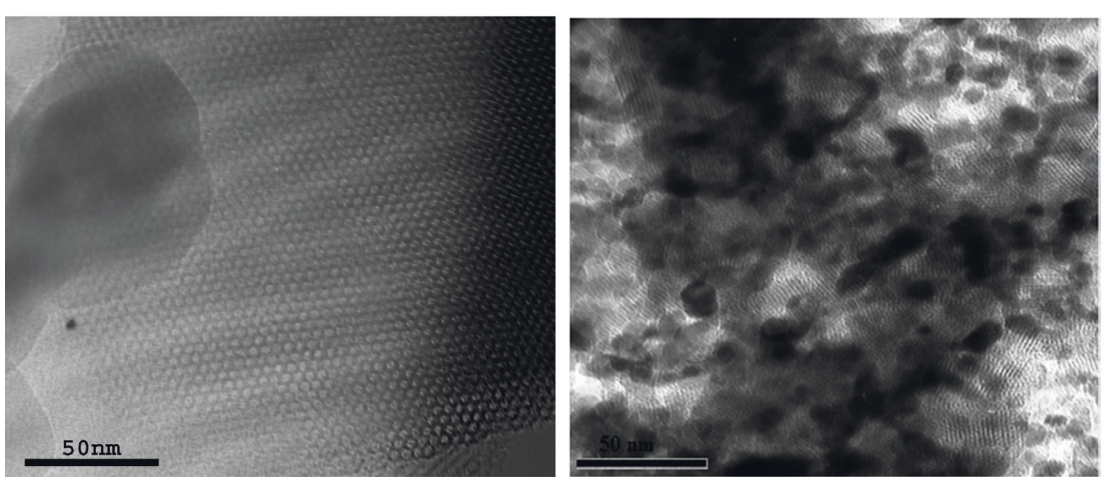

(b)

Figure 6: Continued.

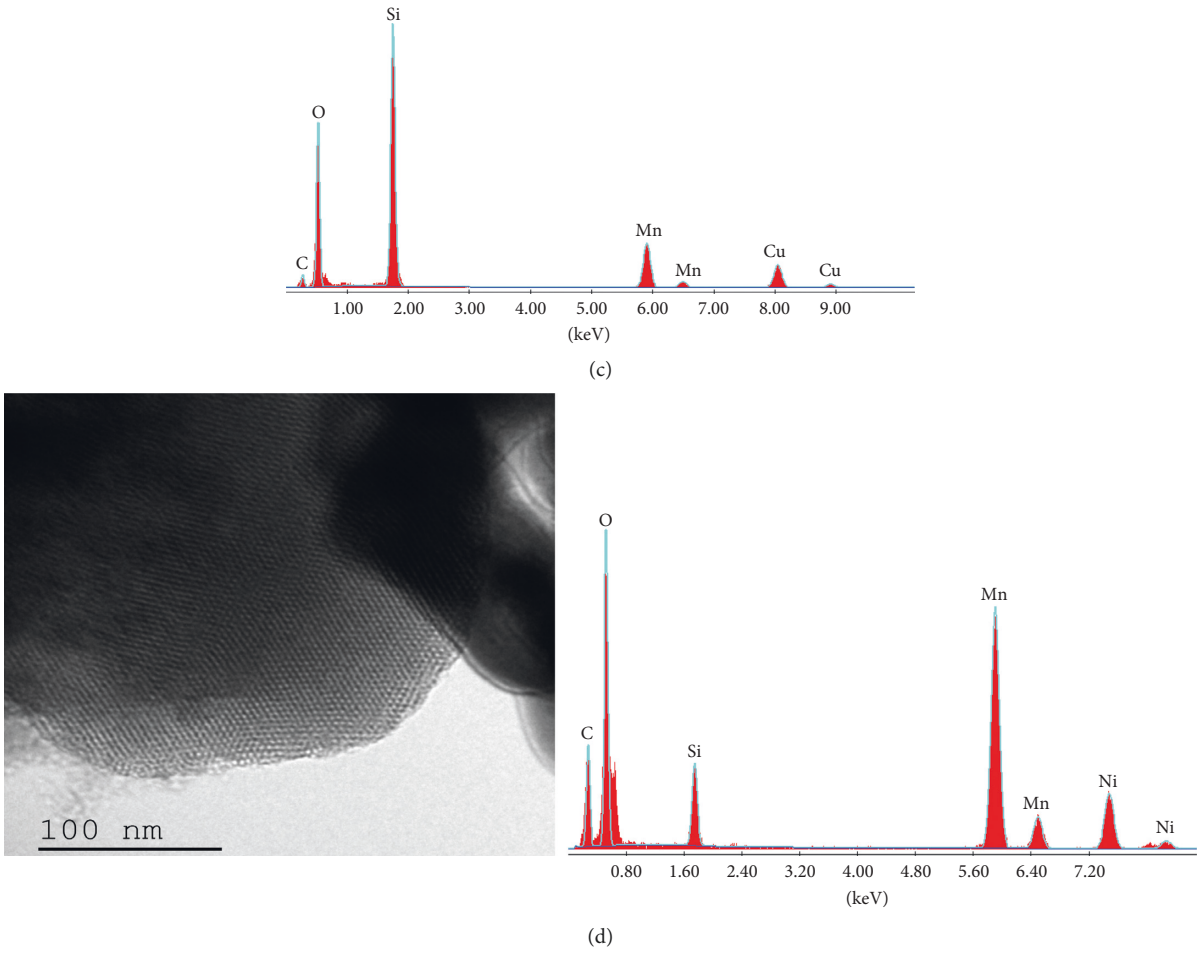

FIGURE 6: TEM images and EDX results of (a) $MnLUS_{DHT}$ (7 wt.%), (b) $MnLUS_{Imp}$ (15 wt.%), (c) $MnLUS_{SSI}$ (15 wt.%), and (d) $MnLUS_{SSI}$ (30 wt.%).

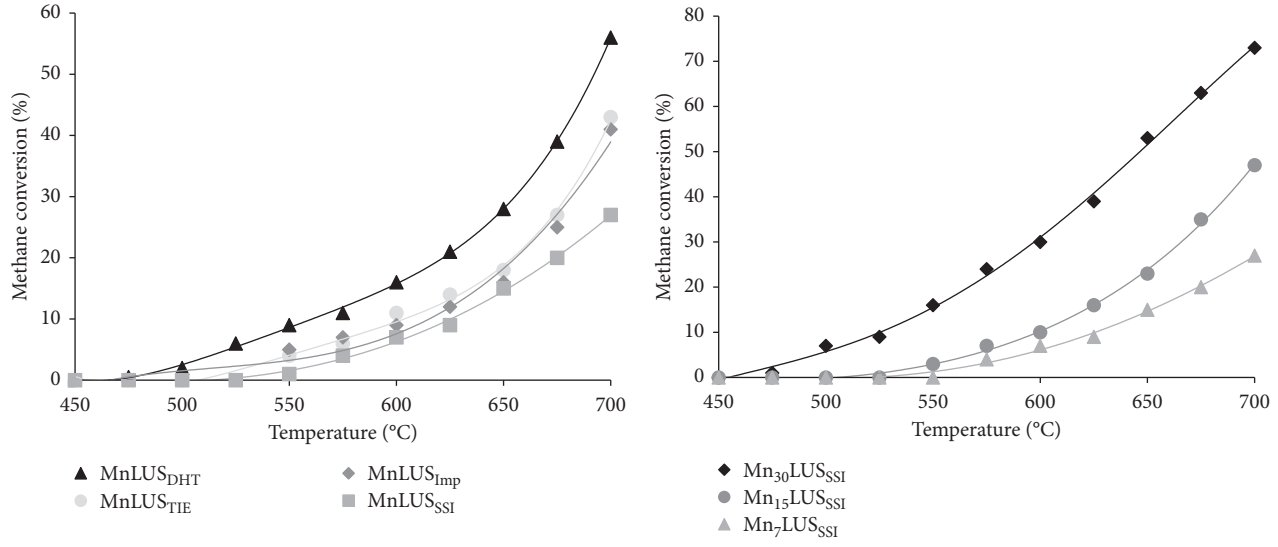

FIGURE 7: Methane conversion as a function of reaction temperature of (a) MnLUS (7 wt.%): $MnLUS_{DHT}$, $MnLUS_{Imp}$, $MnLUS_{TIE}$, and $MnLUS_{SSI}$ and (b) reaction temperature of Mn_7LUS_{SSI}, $Mn_{15}LUS_{SSI}$, and $Mn_{30}LUS_{SSI}$. Mass of the catalyst: 100 mg; gas mixture: $CH_4/O_2/He$ = 1/4/95 (% vol); total flow rate: 100 cm^3 min^{-1}.

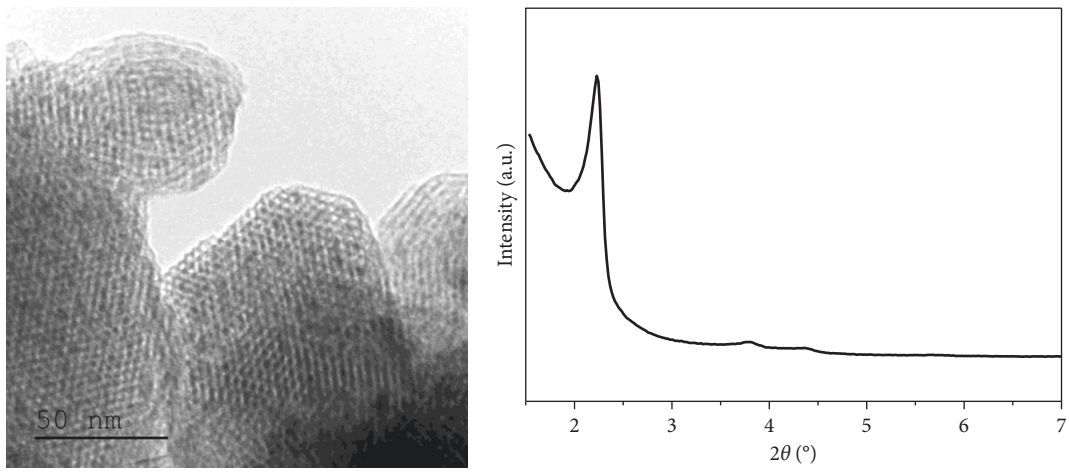

(a) (b)

Figure 8: (a) TEM image of $MnLUS_{SSI}$ and (b) XRD pattern of $MnLUS_{Imp}$ after the catalytic test.

known to depend strongly on its redox properties which are associated with the oxygen storage capacity and oxygen mobility in the oxide lattice since the behavior of manganese oxides in gas-phase oxidation reactions is expected to occur through the Mars–van Krevelen reaction mechanism [45, 46]. In fact, Wasalathanthri et al. [47] have reported that methane can be oxidized by a metal oxide in the absence of gas-phase oxygen, by abstracting lattice oxygen, which results in a reduction of the metal oxide. Thus, more readily reduced surface species have higher redox activities, and according to TPR results, $MnLUS_{SSI}$ is more reducible than the others.

It is important to note that the structure of MnLUS catalysts did not undergo significant change after the catalytic reaction. Indeed, both TEM micrograph and XRD pattern (Figure 8) indicate that the mesoporous structure was maintained, and the catalysts are sufficiently stable during the catalytic reaction.

5. Conclusion

Series of manganese supported on mesoporous materials silica LUS with a 2D hexagonal array of channels were prepared according to DHT, TIE, Imp, and SSI methods, and its physicochemical properties were investigated. The 2D hexagonal structure of LUS remains intact after modification according to XRD, TEM, and N_2 adsorption-desorption which also revealed that manganese is highly dispersed within the channels.

UV-Vis and TPR data exhibited that MnLUS was made up of a mixture of Mn^{3+}, Mn^{4+}, and Mn^{2+} oxo species. The $MnLUS_{DHT}$ sample showed the better catalytic activity compared to other samples prepared with different methods of preparation due to the local environment of manganese incorporated on the surface of mesoporous channels and inside the framework. On the contrary, an increase in manganese loading improves the catalytic activity of samples.

Data Availability

The data used to support the findings of this study are available from the corresponding author upon request.

Conflicts of Interest

The authors declare that they have no conflicts of interest.

Acknowledgments

Thanks to the Tunisian Ministry of Higher Education, Scientific Research and Information and Communication Technologies funds for financial support.

Supplementary Materials

Figure S1: methane conversion as function of time of MnLUS catalysts. Figure S2: graphical abstract. (*Supplementary Materials*)

References

[1] D. Ciuparu, M. R. Lyubovsky, E. Altman, L. D. Pfefferle, and A. Datye, "Catalytic combustion of methane over palladium-based catalysts," *Catalysis Reviews*, vol. 44, no. 4, pp. 593–649, 2002.

[2] T. V. Choudhary, S. Banerjee, and V. R. Choudhary, "Catalysts for combustion of methane and lower alkanes," *Applied Catalysis A: General*, vol. 234, no. 1-2, pp. 1–23, 2002.

[3] Z. Li and G. B. Hound, "A review on complete oxidation of methane at low temperatures," *Journal of Natural Gas Chemistry*, vol. 12, pp. 153–160, 2003.

[4] P. Gélin and M. Primet, "Complete oxidation of methane at low temperature over noble metal based catalysts: a review," *Applied Catalysis B: Environmental*, vol. 39, no. 1, pp. 1–37, 2002.

[5] S. Zribi, B. Albela, L. Bonneviot, and M. S. Zina, "Surface engineering and palladium dispersion in MCM-41 for methane oxidation," *Applied Catalysis A: General*, vol. 502, pp. 195–203, 2015.

[6] C. Amairia, S. Fessi, A. Ghorbel, and A. Rîves, "Methane oxidation behaviour over sol-gel derived Pd/Al2O3-ZrO2 materials: influence of the zirconium precursor," *Journal of Molecular Catalysis A: Chemical*, vol. 332, no. 1-2, pp. 25–31, 2010.

[7] V. R. Choudhary, B. S. Uphade, S. G. Pataskar, and A. Keshavaraja, "Low-temperature complete combustion of methane over Mn–, Co–, and Fe-stabilized ZrO_2," *Angewandte Chemie International Edition in English*, vol. 35, no. 20, pp. 2393–2395, 1996.

[8] J. Li, X. Liang, S. Xu, and J. Hao, "Catalytic performance of manganese cobalt oxides on methane combustion at low temperature," *Applied Catalysis B: Environmental*, vol. 90, no. 1-2, pp. 307–312, 2009.

[9] J. Hu, W. Chu, and L. Shi, "Effects of carrier and Mn loading on supported manganese oxide catalysts for catalytic combustion of methane," *Journal of Natural Gas Chemistry*, vol. 17, no. 2, pp. 159–164, 2008.

[10] A. Bejar, S. Ben Chaabene, M. Jaber, J. F. Lambert, and L. Bergaoui, "Mn-analcime: synthesis, characterization and application to cyclohexene oxidation," *Microporous and Mesoporous Materials*, vol. 196, pp. 158–164, 2014.

[11] H. Pérez, P. Navarro, J. J. Delgado, and M. Montes, "Mn-SBA15 catalysts prepared by impregnation: influence of the manganese precursor," *Applied Catalysis A: General*, vol. 400, no. 1-2, pp. 238–248, 2011.

[12] R. Dula, R. Janik, T. Machej, J. Stoch, R. Grabowski, and E. M. Serwicka, "Mn-containing catalytic materials for the total combustion of toluene: the role of Mn localisation in the structure of LDH precursor," *Catalysis Today*, vol. 119, no. 1–4, pp. 327–331, 2007.

[13] R. Craciun, B. Nentwick, K. Hadjiivanov, and H. Knözinger, "Structure and redox properties of MnOx/Yttrium-stabilized zirconia (YSZ) catalyst and its used in CO and CH_4 oxidation," *Applied Catalysis A: General*, vol. 243, no. 1, pp. 67–79, 2003.

[14] A. Machocki, T. Ioannides, B. Stasinska et al., "Manganese-lanthanum oxides modified with silver for the catalytic combustion of methane," *Journal of Catalysis*, vol. 227, no. 2, pp. 282–296, 2004.

[15] G. Laugel, J. Arichi, M. Molière, A. Kiennemann, F. Garin, and B. Louis, "Metal oxides nanoparticles on SBA-15: efficient catalyst for methane combustion," *Catalysis Today*, vol. 138, no. 1-2, pp. 38–42, 2008.

[16] D. Döbber, D. Kießling, W. Schmitz, and G. Wendt, "MnOx/ZrO2 catalysts for the total oxidation of methane and chloromethane," *Applied Catalysis B: Environmental*, vol. 52, no. 2, pp. 135–143, 2004.

[17] E. Asedegbega-Nieto, E. Díaz, A. Vega, and S. Ordóñez, "Transition metal-exchanged LTA zeolites as novel catalysts for methane combustion," *Catalysis Today*, vol. 157, no. 1–4, pp. 425–431, 2010.

[18] J. Bassil, A. AlBarazi, P. Da Costa, and M. Boutros, "Catalytic combustion of methane over mesoporous silica supported palladium," *Catalysis Today*, vol. 176, no. 1, pp. 36–40, 2011.

[19] A. Gannouni, B. Albela, M. Saïd Zina, and L. Bonneviot, "Metal dispersion, accessibility and catalytic activity in methane oxidation of mesoporous templated aluminosilica supported palladium," *Applied Catalysis A: General*, vol. 464-465, pp. 116–127, 2013.

[20] S. Abry, A. Thibon, B. Albela, P. Delichère, F. Banse, and L. Bonneviot, "Design of grafted copper complex in mesoporous silica in defined coordination, hydrophobicity and confinement states," *New Journal of Chemistry*, vol. 33, no. 3, p. 484, 2009.

[21] N. Lang and A. Tuel, "A fast and efficient ion-exchange procedure to remove surfactant molecules from MCM-41 materials," *Chemistry of Materials*, vol. 16, no. 10, pp. 1961–1966, 2004.

[22] K. T. Ranjit, Z. Chang, R. M. Krishna, A. M. Prakash, and L. Kevan, "Photoinduced charge separation of methylphenothiazine in microporous metal silicoaluminophosphate M–SAPO-n(M = Cr, Fe, Mn,n = 5, 8, 11) materials," *Journal of Physical Chemistry B*, vol. 104, no. 33, pp. 7981–7986, 2000.

[23] E. Mannei, F. Ayari, M. Mhamdi et al., "Ammoxidation of C_2 hydrocarbons over Mo-zeolite catalysts prepared by solid-state ion exchange: nature of molybdenum species," *Microporous and Mesoporous Materials*, vol. 219, pp. 77–86, 2016.

[24] M. Kruk, M. Jaroniec, and A. Sayari, "Adsorption study of surface and structural properties of MCM-41 materials of different pore sizes," *Journal of Physical Chemistry B*, vol. 101, no. 4, pp. 583–589, 1997.

[25] X. Wang, Y. Liu, Y. Zhang et al., "Structural requirements of manganese oxides for methane oxidation: XAS spectroscopy and transition-state studies," *Applied Catalysis B: Environmental*, vol. 229, pp. 52–62, 2018.

[26] H. Na, T. Zhu, Z. Liu, and Y. Sun, "Promoting effect of Zr on the catalytic combustion of methane over Pd/γ-Al2O3 catalyst," *Frontiers of Environmental Science and Engineering*, vol. 8, no. 5, pp. 659–665, 2013.

[27] J. Chaignon, Y. Bouizi, L. Davin, N. Calin, B. Albela, and L. Bonneviot, "Minute-made and low carbon fingerprint microwave synthesis of high quality templated mesoporous silica," *Green Chemistry*, vol. 17, no. 5, pp. 3130–3140, 2015.

[28] W. J. Zhou, B. Albela, M. Y. He, and L. Bonneviot, "Design of a bio-inspired copper (II) Schiff base complex grafted in mesoporous silica for catalytic oxidation," *Polyhedron*, vol. 64, pp. 371–376, 2013.

[29] K. M. Parida and S. S. Dash, "Manganese containing MCM-41: synthesis, characterization and catalytic activity in the oxidation of ethylbenzene," *Journal of Molecular Catalysis A: Chemical*, vol. 306, no. 1-2, pp. 54–61, 2009.

[30] H. Sekkiou, B. Boukoussa, R. Ghezini et al., "Enhanced hydrogen storage capacity of copper containing mesoporous silicas prepared using different methods," *Materials Research Express*, vol. 3, no. 8, article 085501, 2016.

[31] V. A. de la Pena O'Shea, M. C. Alvarez-Galvan, J. Requies et al., "Synergistic effect of Pd in methane combustion PdMnOx/Al2O3 catalysts," *Catalysis Communications*, vol. 8, no. 8, pp. 1287–1292, 2007.

[32] X. Dong, W. Shen, Y. Zhu, L. Xiong, J. Gu, and J. Shi, "Investigation on Mn-loaded mesoporous silica MCM-41 prepared via reducing $KMnO_4$ with in situ surfactant," *Microporous and Mesoporous Materials*, vol. 81, no. 1–3, pp. 235–240, 2005.

[33] A. Derylo-Marczewska, W. Gac, N. Popivnyak, G. Zukocinski, and S. Pasieczna, "The influence of preparation method on the structure and redox properties of mesoporous Mn-MCM-41 materials," *Catalysis Today*, vol. 114, no. 2-3, pp. 293–306, 2006.

[34] N. J. Coville and A. M. Tshavhungwe, "Mesoporous ethanesilica materials with bimodal and trimodal pore-size distributions synthesised in the presence of cobalt ions," *South African Journal of Science*, vol. 106, no. 7-8, 2010.

[35] R. D. Shannon and C. T. Prewitt, "Revised values of effective ionic radii," *Acta Crystallographica Section B Structural*

Crystallography and Crystal Chemistry, vol. 26, no. 7, pp. 1046–1048, 1970.

[36] M. C. Álvarez-Galván, B. Pawelec, V. A. de la Peña O'Shea, J. L. G. Fierro, and P. L. Arias, "Formaldehyde/methanol combustion on alumina-supported manganese-palladium oxide catalyst," *Applied Catalysis B: Environmental*, vol. 51, no. 2, pp. 83–91, 2004.

[37] N. Stamatis, K. Goundani, J. Vakros, K. Bourikas, and C. Kordulis, "Influence of composition and preparation method on the activity of MnOx/Al2O3 catalysts for the reduction of benzaldehyde with ethanol," *Applied Catalysis A: General*, vol. 325, no. 2, pp. 322–327, 2007.

[38] M. Baldi, F. Milella, J. M. Gallardo-Amores, and G. Busca, "A study of Mn-Ti oxide powders and their behaviour in propane oxidation catalysis," *Journal of Materials Chemistry*, vol. 8, no. 11, pp. 2525–2531, 1998.

[39] L. Lamaita, M. A. Peluso, J. E. Sambeth, and H. J. Thomas, "Synthesis and characterization of manganese oxides employed in VOCs abatement," *Applied Catalysis B: Environmental*, vol. 61, no. 1-2, pp. 114–119, 2005.

[40] Q. Zhang, Y. Wang, S. Itsuki, T. Shishido, and K. Takehira, "Manganese-containing MCM-41 for epoxidation of styrene and stilbene," *Journal of Molecular Catalysis A: Chemical*, vol. 188, no. 1-2, pp. 189–200, 2002.

[41] D. P. Goldberg, J. Telser, J. Krzystek et al., "EPR spectra from "EPR-Silent" species: high-field EPR spectroscopy of manganese(III) porphyrins," *Journal of the American Chemical Society*, vol. 119, no. 37, pp. 8722-8723, 1997.

[42] S. Todorova, I. Yordanova, A. Naydenov et al., "Cobalt-manganese supported oxides as catalysts for complete n-hexane and methane oxidation: relationship between structure and catalytic activity," *Revue Roumaine de Chimie*, vol. 59, no. 3-4, pp. 259–265, 2014.

[43] J. Xu, Z. Luan, T. Wasowicz, and L. Kevan, "ESR and ESEM studies of Mn-containing MCM-41 materials," *Microporous and Mesoporous Materials*, vol. 22, no. 1–3, pp. 179–191, 1998.

[44] R. Craciun, "Structure/activity correlation for unpromoted and CeO_2-promoted MnO_2/SiO_2 catalysts," *Catalysis Letters*, vol. 55, no. 1, pp. 25–31, 1998.

[45] Y. F. Han, K. Ramesh, L. Chen, E. Widjaja, S. Chilukoti, and F. Chen, "Observation of the reversible phase-transformation of α-Mn2O3 nanocrystals during the catalytic combustion of methane by in situ Raman spectroscopy," *Journal of Physical Chemistry C*, vol. 111, no. 7, pp. 2830–2833, 2007.

[46] E. R. Stobbe, B. A. de Boer, and J. W. Geus, "The reduction and oxidation behaviour of manganese oxides," *Catalysis Today*, vol. 47, no. 1–4, pp. 161–167, 1999.

[47] N. D. Wasalathanthri, A. S. Poyraz, S. Biswas et al., "High-performance catalytic CH_4 oxidation at low temperatures: inverse micelle synthesis of amorphous mesoporous manganese oxides and mild transformation to K_2-xMn_8O_{16} and ϵ-MnO_2," *Journal of Physical Chemistry C*, vol. 119, no. 3, pp. 1473–1482, 2015.